

Photometric/Spectroscopic Redshift Identification of Faint Galaxies in STIS Slitless Spectroscopy Observations

Hsiao-Wen Chen¹, Kenneth M. Lanzetta¹, and Sebastian Pascarelle¹

Department of Physics and Astronomy, State University of New York at Stony Brook, Stony Brook, NY 11794-3800

Abstract.

We present a new spectrum extraction technique which employs optimal weights for the spectral extraction, deblends the overlapping spectra, determines the precise sky background, and takes into account correlations between errors correctly for STIS slitless observations. We obtained roughly 250 optimally extracted spectra in a deep STIS field as well as self-confirming redshift measurements for these objects, including a galaxy at $z = 6.68$. In addition, we identified five isolated emission-line objects in the dispersed image that were not accounted for by objects detected in the direct image. Assuming that these are Ly α emission line galaxies at high redshifts and adopting a simple δ -function galaxy luminosity function for these objects, we find, based on a likelihood analysis, that Ly α emission line galaxies at $\langle z \rangle \approx 4.69$ may contribute at most 15% of the star formation rate density measured in Lyman break galaxies at $z \approx 4$.

1. Introduction

Observations of distant galaxies have advanced rapidly as a result of the Keck telescope, which because of its large collecting area is sensitive to faint objects. But despite extensive searches, only four galaxies of redshift $z > 5$ have as yet been identified spectroscopically using the Keck telescope (Dey et al. 1998; Hu, McMahon, & Cowie 1998; Weymann et al. 1998; Spinrad et al. 1998). It has proven extremely difficult to identify high-redshift galaxies solely based on ground-based spectroscopy, because (1) galaxies lack prominent narrow-band features at rest-frame ultraviolet wavelengths (which are redshifted to observed-frame optical or infrared wavelengths) and (2) background sky light is the dominant source of noise at near-infrared wavelengths.

We have sought to identify distant galaxies in very deep slitless spectroscopy observations acquired by STIS on board HST, by combining a new spectrum extraction technique with photometric and spectroscopic analysis techniques. Our analysis was designed to identify redshifts of galaxies in the slitless data by means of broad-band photometric techniques and to test these redshifts by identifying narrow-band emission, absorption, and continuum features in the same spectra. As a result of this analysis, we obtained optimally extracted spectra and self-confirming redshift measurements for roughly 250 object, including a galaxy at $z = 6.68$, and 5 isolated emission-line objects.

2. Data

The very deep observations, obtained by HST using STIS toward a region of sky flanking the Hubble Deep Field, consisted of pairs of images: a direct image taken using no filter and a dispersed image taken using the G750L grating. Additional observations consisted of only a direct image. The integration time of the direct images totaled 4.5 h over 82 exposures, and the integration time of the dispersed images totaled 13.5 h over 60 exposures. We summed the direct and dispersed images using conventional image processing techniques. The summed image covers a sky area of 51×51 arcsec². The spatial resolution of the summed direct and dispersed images is FWHM ≈ 0.08 arcsec, the 1σ detection threshold of the summed direct image is ≈ 26.2 mag arcsec⁻², and the 1σ detection threshold of the summed dispersed image at $\lambda \approx 9800$ Å is $\approx 5.5 \times 10^{-18}$ erg s⁻¹ cm⁻² Å⁻¹ arcsec⁻¹.

3. Optimal Extraction of Slitless Spectra

The spectrum extraction of the dispersed image is made especially difficult because the image of the field is covered by light of faint galaxies, which when dispersed overlaps in the spatial direction and is blurred in the spectral direction. To spatially deblend and spectrally deconvolve the spectra, we used the summed direct image to determine not only the exact object locations but also the exact two-dimensional spatial profiles of the spectra on the summed dispersed image. The spatial profiles of these objects are crucial because (1) they provide the “weights” needed to optimally extract the spectra, (2) they provide the models needed to deblend the overlapping spectra and determine the background sky level, and (3) they provide the spectral templates needed to optimally deconvolve the spectral blurring of extended objects.

First, we identified objects in the summed direct image, using the SExtractor program of Bertin & Arnouts (1996). Roughly 250 objects were identified in the summed direct image. Next, we modeled each pixel (i, j) of the summed dispersed image as a linear sum of contributions from (1) relevant portions of all overlapping neighboring objects and (2) background sky:

$$\mathcal{F}_{i,j} = \sum_k S_{i-i_k-\Delta+1}^k \sum_{i''_k} f_{i''_k-i''_k,j}^k + B_{i,j}, \quad (1)$$

where S_l^k are spectral elements of the k th object, i_k is the object position along the spectral direction in the direct image, Δ is the constant offset between object position and the starting pixel of the spectrum along the spectral direction, f is the object profile measured in the direct image, and B is the model sky (for which we found that a fourth order polynomial is necessary and sufficient).

We treated the problem as a χ^2 minimization problem, where the data were the pixel values of the summed dispersed image, the model was a linear sum of appropriate elements of the spatial profiles, and the parameters of the model were values of the spectral pixels. The χ^2 is written

$$\chi^2 = \sum_{i,j} \frac{(\mathcal{F}_{i,j} - \tilde{\mathcal{F}}_{i,j})^2}{\sigma_{i,j}^2}, \quad (2)$$

where $\tilde{\mathcal{F}}_{i,j}$ is the flux measurement and $\sigma_{i,j}$ is the 1- σ error at pixel (i, j) .

Finally, we minimized χ^2 between the model and the data with respect to the model parameters and obtained estimates of all model parameters simultaneously to form one-dimensional spectra. The model parameters included roughly 250,000 “object” parameters (from roughly 1000 spectral pixels each of roughly 250 objects) and four thousand more “sky” parameters. As a zeroth order approximation, the spectral elements of individual objects are independent of each other, and so we can solve the minimum χ^2 separately for individual columns. The χ^2 for column i is

$$\chi_i^2 = \sum_j \frac{\left(\sum_k S_{i-i_k-\Delta+1}^k \sum_{i_k''} f_{i_k-i_k'',j}^k + \sum_{\alpha=0}^L a_i^\alpha j^\alpha - \tilde{\mathcal{F}}_{i,j} \right)^2}{\sigma_{i,j}^2}. \quad (3)$$

Now we only need to solve for approximately 250 spectral elements S_l^k and $(L+1)$ sky parameters a_i^α (here $L = 4$) that give the minimum χ_i^2 each time and repeat the calculation for all columns. Errors of the model parameters were obtained by solving the Hessian matrix at the minimum χ_i^2 .

This new spectrum extraction method is superior to other extraction methods in many ways. First, the method employs optimal weights for the spectral extraction. Second, the method deblends the spectra. Third, the method determines the precise sky background. Because the dispersed image is covered by light of extremely faint galaxies over most of its area, the spatial templates are needed to find the rare “clear” regions of sky background between the object spectra. Finally, the method estimates errors correctly by taking into account the correlation between spectral elements of overlapping objects.

As a result of the spectrum extraction technique, we obtain 250 optimally extracted spectra for redshift analysis. To determine redshifts of extremely faint galaxies in STIS slitless spectra, we first measured photometric redshifts by means of a redshift likelihood technique (Fernández-Soto, Lanzetta, & Yahil 1999) and verified these redshifts by identifying narrow-band emission, absorption, and continuum features in the same spectra. The goal is to obtain self-confirming photometric redshift estimates.

4. Noise Characteristics

The new spectrum extraction technique adopts object profiles determined from the direct image as model templates to determine the exact sky and to optimally extract spectra from the dispersed image. The analysis involves complicated smoothing and deblending. It is therefore not unreasonable to expect that the noise characteristics may have been highly skewed in the extracted spectra and do not follow a normal distribution any more. To proceed with discussions on the significance of detections of any spectral features, it is indeed necessary for us to first understand the noise characteristics of the final products of the analysis.

To examine the noise characteristics, we form a histogram of pixel values of about 15 rows randomly chosen from the residual image. The histogram is shown in Figure 1, in which we also plot the best-fit Gaussian distribution with

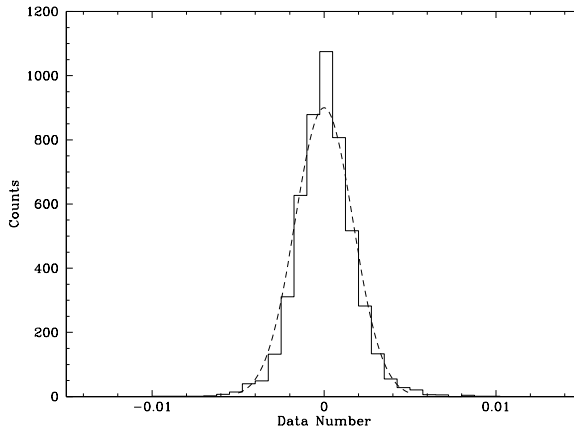


Figure 1. Histogram of noise in the residual image. The dashed curve indicates a best-fit Gaussian profile.

the full width at half maximum of 0.004. The corresponding $1\text{-}\sigma$ deviation is 0.0017, which is slightly larger than the $1\text{-}\sigma$ deviation measured in the dispersed image (0.0015). The fact that the noise in the residual image follows a Gaussian distribution with a slightly larger $1\text{-}\sigma$ deviation has secured our subsequent reference to a normal noise distribution for any further statistical analysis.

5. Properties of Isolated Emission Lines

In addition to the 250 objects observed in the direct image, which included a galaxy at $z = 6.68$, we identified five isolated emission lines in the dispersed image that were not accounted for by objects detected in the direct image. The $z = 6.68$ galaxy is the most distant galaxy that has yet been spectroscopically identified. Detailed analysis has been presented elsewhere (Chen, Lanzetta, & Pascarella 1999). Here we focus on the five emission-line objects.

To objectively identify these isolated emission lines, we applied the SExtractor program to the smoothed dispersed image, setting the detection threshold such that nothing was detected in the negative of the image. Next, we removed the lines that correspond to objects identified in the direct image. Consequently, five isolated emission lines remained in the dispersed image.

The nature of these isolated emission lines is uncertain because of the ambiguities in the wavelength determination. It is impossible to determine the wavelengths and therefore to calibrate the fluxes for these lines without first knowing their positions on the sky. We show in Figure 2 that the $1\text{-}\sigma$ flux threshold of an unresolved emission line in the dispersed image may vary with wavelength by as much as a factor of four across the entire spectral range. However, given the $1\text{-}\sigma$ single pixel detection threshold of the direct image, $\approx 26.2 \text{ mag arcsec}^{-2}$, we can work out the $3\text{-}\sigma$ lower limit to the observed equivalent width (EW) as a function of wavelength for these isolated emission lines. The dot-dashed curve in Figure 2 indicates the $3\text{-}\sigma$ lower limit to the observed EW of an unresolved line detected at a $3\text{-}\sigma$ significance level in the dispersed image versus wavelength. The actual observed EW limit as a function of wavelength

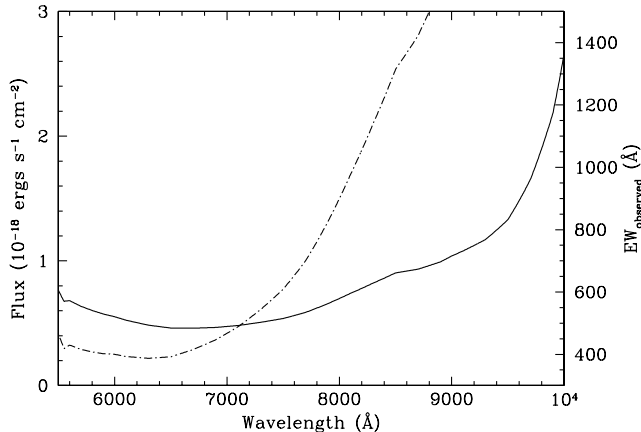


Figure 2. The solid curve is the $1\text{-}\sigma$ flux threshold of an unresolved emission line in the dispersed image versus wavelength. The dot-dashed curve shows the $3\text{-}\sigma$ lower limit to the observed equivalent width.

for a particular line can be obtained by scaling the dot-dashed curve to the significance of the line detection. According to the EW limits shown in Figure 2, the observed five emission lines are most likely to be high-redshift Ly α emission lines, rather than low-redshift [O II] or H α lines.

The sensitivity curve shown in Figure 2 also indicates that the STIS observations are more sensitive to faint emission-line galaxies than existing deep narrowband surveys from the ground (e.g. Hu, Cowie, & McMahon 1998). If these lines are high-redshift Ly α emission lines, the statistics drawn from this observation may place a strong constraint on the number density of high-redshift Ly α emission line galaxies and the star formation rate density contributed by this population. However, the study has been made extremely difficult because of the ambiguities in the wavelength (and therefore redshift) determination.

To solve this problem, we applied a likelihood analysis to the observed emission lines, assuming that all five emission lines are high-redshift Ly α lines and that the number density of these lines is well represented by a simple δ -function luminosity function,

$$\phi(L/L_*) = \phi_* \delta(L/L_* - 1). \quad (4)$$

The likelihood analysis returns a best-fit characteristic luminosity $L_* = 0.4 \times 10^{42} h^{-2} \text{ergs s}^{-1}$. Given the fact that five lines were detected, we find the number density to be $\phi_* = 0.04 h^3 \text{Mpc}^{-3}$.

On the basis of the simple δ -function galaxy luminosity function determined for the observed Ly α emission line objects, we estimated the statistical properties of the galaxy population. First, we calculated the mean redshift of the observed lines and found $\langle z \rangle = 4.69$. Second, we estimated the star formation rate density, using the relationship between H α luminosity and star formation rate of Madau, Pozzetti, & Dickinson (1998) and assuming case B recombination, where Ly α /H $\alpha \approx 10$ (Osterbrock 1989). It turns out that the star formation rate density of Ly α emission line galaxies is $0.01 h M_\odot \text{yr}^{-1} \text{Mpc}^{-3}$ for $q_0 = 0.5$ (without correction for extinction). This is about 15% of the star formation rate density

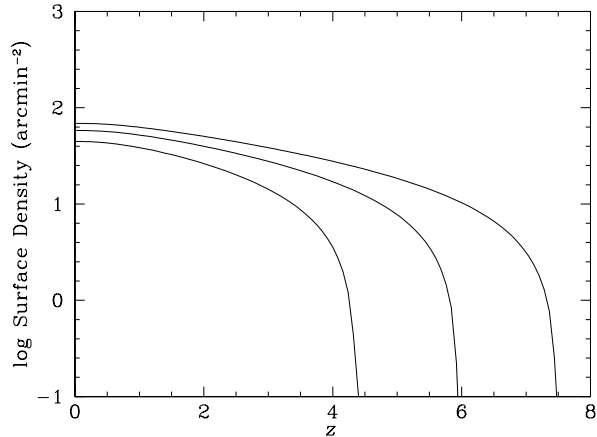


Figure 3. The predicted surface density of Ly α emission line galaxies at different detection thresholds. The curves, from bottom up, correspond to a threshold of 10 , 5 , and 3×10^{-18} ergs s $^{-1}$ cm $^{-2}$, respectively.

measured by Steidel et al. (1999) for the Lyman break galaxies at $z > 4$, suggesting that galaxies exhibiting the Ly α emission feature represent only a small portion of the whole galaxy population at high redshifts. We therefore conclude that high-redshift galaxies are more efficiently and objectively identified using broad-band photometric rather than narrow-band imaging/spectroscopic techniques.

Finally, we calculated the surface density of Ly α emission line galaxies expected in observations of a given sensitivity. Figure 3 shows that we expect to detect no more than five Ly α emission line galaxies per arcmin 2 at $z > 4$ that are stronger than 1×10^{-17} ergs s $^{-1}$ cm $^{-2}$ and no more than 10 Ly α emission line galaxies per arcmin 2 at $z > 5$ that are stronger than 5×10^{-18} ergs s $^{-1}$ cm $^{-2}$.

Acknowledgments. This research was supported by NASA grant NACW-4422 and NSF grant AST-9624216.

References

- Bertin, E. & Arnouts, S. 1996, A&AS, 117, 393
Chen, H.-W., Lanzetta, K. M., & Pascarella, S. 1999, Nature, 398, 586
Dey, A. et al. 1998, ApJ, 498, L93
Fernández-Soto, A., Lanzetta, & Yahil, A. 1999, ApJ, 513, 34
Hu, E. M., Cowie, L. L., & McMahon, R. G. 1998, ApJL, 502, 99
Madau, P., Pozzetti, L., & Dickinson, M. 1998, ApJ, 498, 106
Osterbrock, D. E. 1989, Astrophysics of Gaseous Nebulae and Active Galactic Nuclei (University Science Books: California)
Spinrad, H. et al. 1998, AJ, 116, 2617
Steidel, C. C. et al. 1999, ApJ, in press (astro-ph/9811399).
Weymann, R. J. et al. 1998, ApJL, 505, 95